Wind and Structures, *Vol. 29, No. 3 (2019) 149-161*
DOI: https://doi.org/10.12989/was.2019.29.3.149

Dynamic response of railway vehicles under unsteady aerodynamic forces caused by local landforms

Zhengwei Chen[1,2,3], Tanghong Liu*[1,2,3], Ming Li[4], Miao Yu[4], Zhaijun Lu[1,2,3] and Dongrun Liu[1,2,3]

[1]*Key Laboratory of Traffic Safety on Track of Ministry of Education, School of Traffic & Transportation Engineering, Central South University, Changsha 410075, P.R. China*
[2]*Joint International Research Laboratory of Key Technology for Rail Traffic Safety, Changsha 410075, P.R. China*
[3]*National & Local Joint Engineering Research Center of Safety Technology for Rail Vehicle, Changsha 410075, P.R. China*
[4]*P&T Research Center, CRRC Tangshan Co., Ltd., Tangshan 063035, P.R. China*

(Received July 6, 2018, Revised May 1, 2019, Accepted July 6, 2019)

Abstract. When a railway vehicle runs in crosswinds, the unsteady aerodynamic forces acting on the train induced by the vehicle speed, crosswind velocity and local landforms are a common problem. To investigate the dynamic performance of a railway vehicle due to the influence of unsteady aerodynamic forces caused by local landforms, a vehicle aerodynamic model and vehicle dynamic model were established. Then, a wind-loaded vehicle system model was presented and validated. Based on the wind-loaded vehicle system model, the dynamic response performance of the vehicle, including safety indexes and vibration characteristics, was examined in detail. Finally, the effects of the crosswind velocity and vehicle speed on the dynamic response performance of the vehicle system were analyzed and compared.

Keywords: railway vehicle; unsteady aerodynamic forces; dynamic performance; landforms

1. Introduction

With the development of high-speed railway technology, high-speed trains have become increasingly important in recent years. Meanwhile, the requirements for safety, speed, and efficiency of trains have become more stringent; these requirements greatly depend on the dynamic vehicle characteristics of stability and safety. In practice, operating railway vehicles are sensitive to various disturbances including unsteady aerodynamic forces and railway curve (Niu *et al*. 2015). In an extreme environment, the dynamic performance of a train vehicle worsens, with increased risk of derailment or overturning. Some train overturning accidents have occurred in China, Japan, Belgium and Switzerland due to strong crosswinds (Xiao *et al*. 2011, Baker *et al*. 2009).

The unsteady aerodynamic force is an important factor in the safe operation of railway vehicles. Many researchers have studied related problems, including vehicle dynamic analysis and determining the crosswind influence on the vehicle dynamics. Wu *et al*. (2015, 2017) studied the sudden load-off and load-on the railway vehicle phenomenon under crosswind in the bridge, which is caused by the wind shielding effects of bridge tower and the artificial discrete simulation of wind field. The results indicated that the sudden changes of aerodynamics loads have a large impact on the dynamic performance of the running railway vehicle. Similarly, considering tower shielding and triangular wind barriers in the bridge, Zhang *et al*. (2015) proposed a method to analyze the wind-vehicle-bridge system, the static wind load and the buffeting wind load for both the bridge and the vehicle are included. Using mutually-affected aerodynamic parameters, Wang *et al*. (2015) investigated the dynamics analysis of wind-vehicle-bridge systems, it showed that obvious lateral and yaw motions of the road vehicle occur. Other people, including Zhai *et al*. (2015), Guo *et al*. (2015), Zhang *et al*. (2013), Cui *et al*. (2014) also investigated the running safety and dynamics of train on bridge under crosswind.

Except the train runs in the bridge, the equivalent crosswind load, which is calculated using computational fluid dynamics (CFD), can be used in simulations to consider the overturning risk when a vehicle is running in a curve or other conditions under a crosswind or even a crosswind gust (Thomas *et al*. 2010). Hosoi and Tanifuji (2012) studied the influence of crosswind on derailment of a train in a curve track, and suggested a crosswind safety allowance and a specific train speed using simulations. For the device above the roof, the influence of aerodynamic forces on the pantograph-catenary system was studied by Pombo *et al*. (2009) using an off-line coupled method. This co-simulation of a finite element model and a multi-body system with nonlinear crosswind forces showed that a crosswind can raise the pantograph, increase the contact forces, and increase the range of variation of the contact forces.

As mentioned above, the effects of aerodynamic forces on the dynamic performance of a railway vehicle have been researched in some studies. But it can be seen that there are few studies focus on effect of the real complex terrain on the train safety under crosswind. In China, Lanzhou-

*Corresponding author, Professor
E-mail: lth@csu.edu.cn

ISSN: 1226-6116 (Print), 1598-6225 (Online)

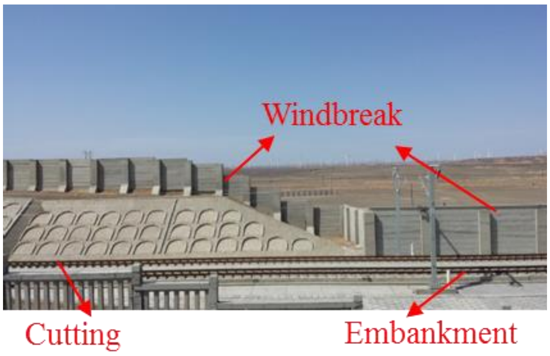

(a) Structure toward rail line

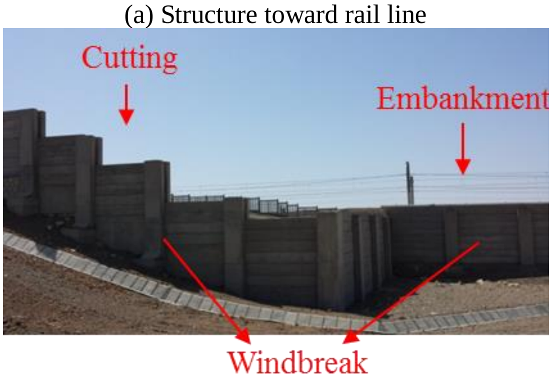

(b) Structure outward rail line

Fig. 1 Windbreak rectangular transition between cutting and embankment

Xinjiang railway passes through a gale region with a severe crosswind environment. Some researchers have studied the influence of strong crosswinds on the risk of overturning (Liu *et al*. 2016). Wind barriers are the main method that is used to ensure traffic safety, especially under strong crosswinds (Ogueta-Gutiérrez *et al*. 2014). Certain features, such as windbreak setting, shape, wind speed and vehicle speed, have been extensively researched for plat ground, embankments, and viaducts in previous studies (Catanzaro *et al*. 2016, Avila-Sanchez *et al*. 2014). The literature shows that the conditions studied in the past were idealized, and different scenarios were studied separately. However, in an actual railway line, because of the effects of complex terrain conditions, a windbreak is built discontinuously. In a full-scale test, Lu *et al*. (2014) found that the aerodynamic performance and dynamic index of a vehicle system showed sudden changes and frequently became worse solely in the position of the discontinuous transition region of windbreak. For example, part of the Lanzhou–Xinjiang passenger railway line that passes through the strong wind area is in mountainous terrain, which also results in many cuttings, embankments, and transition regions along this line, as shown in Fig. 1. When trains pass through this windbreak transition region, a 'yawing' phenomenon occurs, affecting both passenger comfort and operational safety.

There are few studies investigated this problem, and it is necessary to understand the specific effect of this new problem on the train safety. Therefore, the present study analyzes the dynamic response performance and operational safety of a train under crosswind passing through the rectangular windbreak transition region considering the actual terrain around the railway, and provides the reference for the further optimization and reconstruction of windbreak structure in this transition region.

2. Computational model and method

2.1 Vehicle aerodynamic model

2.1.1 Model description

The train model studied in the present work is the China Railway High-Speed 2 (CRH2), which was tested on Lanzhou-Xinjiang railway. To simulate the actual operation, a realistic three-dimensional landform, as shown in Fig. 2(a), is established to compute the unsteady aerodynamic forces acting on the vehicle. The landform includes windbreak structures, a cutting, an embankment and the distant terrain around the railway line. The basic railway sizes as shown in Figs. 2(a) and 2(b). In addition, as shown in Fig. 2(c), a CRH2 model is established. Considering the computational efficiency and the aim of the present work, the pantograph-catenary system is neglected, and the train model is simplified to 3 cars: C1 - lead car, C2 - middle car, and C3 - tail car.

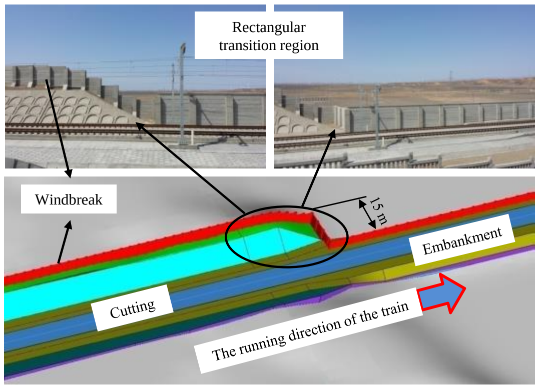

(a) The actual landform and model

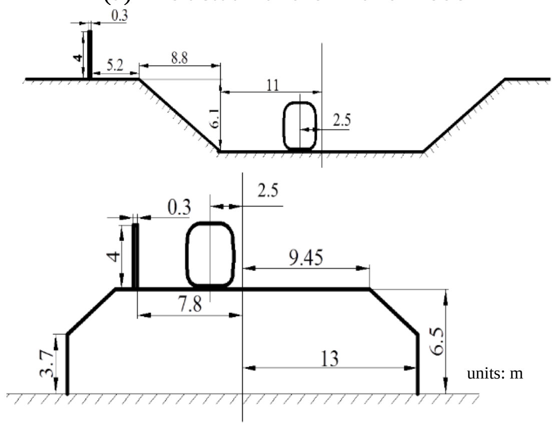

(b) Cutting and embankment

(c) The CRH2 model

Fig. 2 The aerodynamic models

2.1.2 Numerical method and model setup

In terms of crosswind/train aerodynamics, the $k-\varepsilon$ turbulent model is extensively applied due to the effectiveness and reliability. The standard $k-\varepsilon$ turbulent model is the simplest and most adaptable model for simple geometry and flow (Pope 2000), and is extensively employed for flows with a high Reynolds number. The components of the Reynolds stress for the standard $k-\varepsilon$ turbulent model are isotropic; this hypothesis is not realistic. To remedy this flaw, a RNG $k-\varepsilon$ turbulent model was developed by Yakhot and Orszag (1986). The RNG $k-\varepsilon$ turbulent model differs from the standard $k-\varepsilon$ turbulent model, which considers the rotational flow in the mean flow by amending the turbulence viscosity. It has an additional term in the function and reflects the main flow time-average strain rate. These improvements increase the credibility and accuracy of the RNG $k-\varepsilon$ turbulent model in an extensive flow field analysis. Therefore, a three-dimensional, incompressible unsteady Reynolds averaged Navier–Stokes (URANS) equations, the RNG $k-\varepsilon$ two-equation turbulent model, and decomposed sliding mesh method are utilized in this paper. The governing equations of the RNG $k-\varepsilon$ turbulent model are described as follows:

Turbulent kinetic energy k equation

$$\frac{\partial(\rho k)}{\partial t}+\frac{\partial(\rho k u_i)}{\partial x_i}=\frac{\partial}{\partial x_j}\left[\alpha_k \mu_{eff}\frac{\partial k}{\partial x_j}\right]+G_k+\rho\varepsilon \quad (1)$$

Turbulent dissipation rate ε equation

$$\frac{\partial(\rho\varepsilon)}{\partial t}+\frac{\partial(\rho\varepsilon u_i)}{\partial x_i}=\frac{\partial}{\partial x_j}\left[\alpha_\varepsilon \mu_{eff}\frac{\partial \varepsilon}{\partial x_j}\right]+\frac{C_{1\varepsilon}^{*}\varepsilon}{k}G_k-C_{2\varepsilon}\rho\frac{\varepsilon^2}{k} \quad (2)$$

Where ρ is the air density, u_i is the velocity component in the i direction; $\alpha_k=\alpha_\varepsilon=1.39$ is the turbulent Prandtl number in the k equation and the ε equation, respectively; μ_{eff} is the effective dynamic viscosity; G_k is the generation of the turbulent kinetic energy by the mean velocity gradients; $C_{1\varepsilon}^{*}$ and $C_{2\varepsilon}$ are model coefficients, where $C_{2\varepsilon}$=1.68.

The commercial software package Fluent 6.3.26 is used in this study, and the governing equations are discretized using the finite volume method (FVM). The convection and diffusion terms are discretized using the second-order upwind scheme, and the time derivative is discretized using the second-order implicit scheme for unsteady flow calculations. The velocity-pressure coupling and solution procedure are based on the SIMPLE algorithm.

In order to satisfy the grid size requirements, the aerodynamic model for the computation in the present work is a 1/10 scaled model, while the descriptions in the following sections are still full-scale dimension for the intuitive and easy understanding. Fig. 3 shows the CFD domain and the boundary conditions. For simplicity, the height of the train model, which is 3.7 m, is taken as the characteristic dimension and is denoted by H. The height of the computational domain is 40.5 H. The length from face EFGH to the nose of the lead car is 180 H; the length from

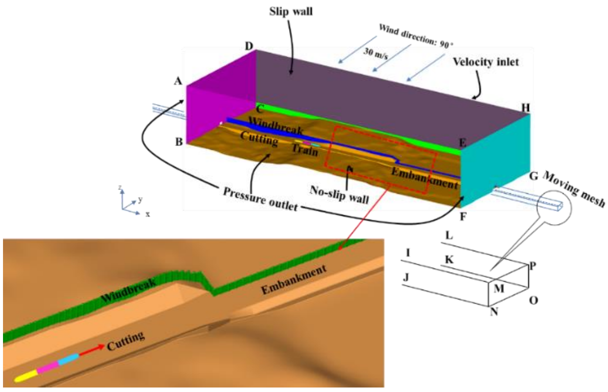

Fig. 3 The computational model setup

face ABCD to the nose of the tail car is 40 H; the length from face ABFE and face DCGH to the longitudinal centre of the train are all 54 H. The boundary conditions are set based on the research in this paper. Face DCGH is a velocity inlet, in order to simulate the nature wind characteristics, the velocity inlet is set as $u=\left(\frac{z}{z_{10}}\right)^{\alpha}u_{10}$, where u is the wind speed in the height of Z, and u_{10} is standard wind speed (the wind speed in the reference height Z_{10}), in China, the wind speed in the height of 10 m is defined as standard wind speed (Huang and Wang 2008). So here Z_{10}=10 m, and u_{10}= 10 m/s to 50 m/s will be analyzed in this paper. α is the ground roughness factor and here α = 0.12 (GB 50009 2003); faces ABCD, ABFE and EFGH are set as pressure outlets; the upper face AEHD is a slip wall; the lower face BFGC and surface of the train is a no-slip wall. Moving mesh technology is used to appropriately simulate the relative motion between the train and the ground, and a stationary train speed is set for the moving mesh, which is defined as IJKL-MNOP. The boundary conditions of faces IJKL and MNOP are pressure outlets, and the remaining faces have interface boundary conditions.

2.1.3 Computational mesh

A tetrahedral grid is used to fill the complex geometry of the domain due to its characteristic advantage of treating complicated objects. The regions around the train and windbreak are refined with a higher grid resolution to ensure accurate results because in which high velocity gradients are expected. In addition, to obtain mesh-independent results, numerical simulations are performed with three different meshes: coarse, medium and fine.

Under the strong wind environment, the pressure distribution of train surface affects the train aerodynamic forces directly, therefore, the pressure coefficients with different meshes are chosen to analyze the mesh sensitivity. Fig. 4 shows the pressure coefficients C_p results from the three meshes around the centre cross-section of the middle car, when the train is held stationary in the cutting with a 30 m/s crosswind. C_p is defined below

$$C_p=\frac{P-P_0}{0.5\rho u^2} \quad (3)$$

where P_0 is the reference pressure, which is 0, and P is the static pressure on the train surface. It can be seen that the medium mesh results closely match the fine mesh, whereas the coarse mesh clearly differ from the others. Therefore, the resolution of the medium mesh is adequate, and no further mesh refinement is performed. Other cross-sections have similar grid independence characteristics but are not elaborated upon here. Therefore, the intermediate mesh is chosen for the following simulations. Fig. 5 shows the mesh around the train model, and where the mesh is refined around the complicated streamline head in order to obtain more accurate results in this area.

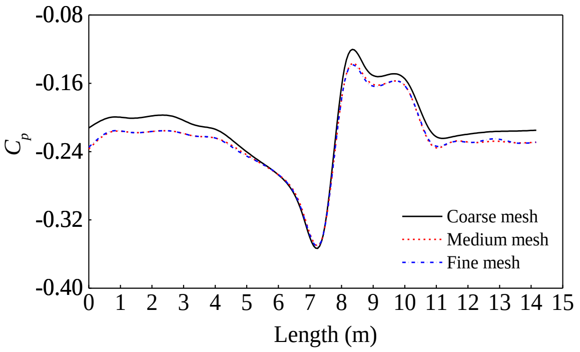

Fig. 4 Pressure coefficient curves with different mesh resolutions

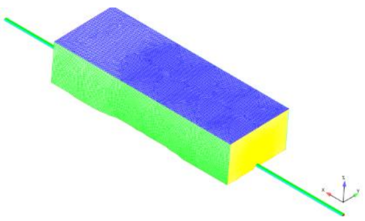

(a) The mesh of the computational domain

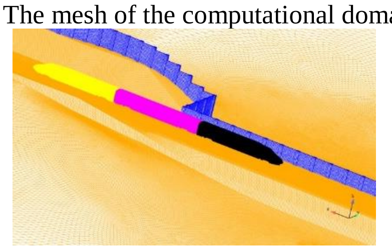

(b) The mesh around the transition region

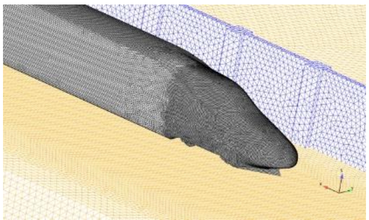

(c) The magnification of train surface mesh

Fig. 5 The computational mesh

2.2 The vehicle multi-body system dynamic model and track model

The vehicle aerodynamic model results only reflect the aerodynamics performance of the vehicle, but the vehicle operation stability and safety cannot be obtained, therefore, the aerodynamic results need be combined with the vehicle system dynamics model to get the results that can assess the train safety directly, such as the derailment coefficient, the overturning coefficient, etc. This section outlines the vehicle multi-body system dynamic model and the track model based on the multi-body system dynamic software SIMPACK (Zhai *et al*. 2009). The subsystems of the vehicle system dynamic model include the car body system, bogie system, and the coupler and draft gear system. In this study, these subsystems are regarded as rigid bodies that are connected by joints or constraints, and the track model is defined as inertia fixed rails.

2.2.1 Vehicle model

In accordance with the vehicle aerodynamic model, the vehicle dynamic model is also established with 3 cars. The lead car and tail car are vehicles with power bogies, and the middle car is a trailer without power. Generally, for the power bogie, the dynamic influence of the traction motor on the vehicle multi-body system is insignificant. Therefore, in this study, the joint and constraint of the traction motor are ignored, but the weight is considered; the weights of the power bogie and trailer bogie differ slightly. Table 1 shows the dynamic parameters of the vehicle model, and Figs. 6(a) and 6(b) show the model of the bogie and vehicle established in SIMPACK; a single vehicle model contains a car body, two bogies, and four pairs of wheelsets. The primary suspension between the wheelset and bogie frame contains a helical spring, a vertical damper and an axle-box. The second suspension between the bogie frame and the car body contains two air springs, a lateral damper, a longitudinal damper (Anti yaw motion damper), and a lateral bump stop. The adjacent car bodies are linked by dampers, couplers and draft gears, and the model established here based on the typical vehicle system dynamics model refer to the reference Iwnicki (2006) and Zhai *et al*. (2009). Considering the constant speed of the vehicle and the vehicle model researched in this study runs on a linear track without curves, the longitudinal acceleration is smaller compared to other directions. And the present work focuses on the effect of crosswind on the train's operation safety, it mainly depends on the lateral and vertical vibration. Therefore, the longitudinal vibration is not analyzed in the section of results discussion. In this study, the vehicle operation direction is the positive *x*-axis, the direction to the right of the vehicle operation is the positive *y*-axis, and the positive *z*-axis is downward.

The vehicle multi-body system components are all regarded as rigid bodies; for a single vehicle, Table 2 lists the degrees of freedom (DOFs) of the vehicle. Each car body, bogie frame and a pair of wheelsets has 6 DOFs, respectively. Therefore, a single vehicle has 42 DOFs; adding the DOFs of the coupler, a model with three vehicles has 128 DOFs.

Table 1 Primary parameters for the vehicle model

Parameter	Value
Car body mass	26,100 kg
Mass moment of inertia of the car body about the *x*-axis	84,560 kg·m^2
Mass moment of inertia of the car body about the *y*-axis	1,278,900 kg·m^2
Mass moment of inertia of the car body about the *z*-axis	1,102,730 kg·m^2
Mass of the frame	2600 kg
Mass moment of inertia of the frame about the *x*-axis	2106 kg·m^2
Mass moment of inertia of the frame about the *y*-axis	1424 kg·m^2
Mass moment of inertia of the frame about the *z*-axis	2600 kg·m^2
Wheelset mass	2100 kg
Mass moment of inertia of the wheelset about the *x*-axis	756 kg·m^2
Mass moment of inertia of the wheelset about the *y*-axis	84 kg·m^2
Mass moment of inertia of the wheelset about the *z*-axis	1029 kg·m^2
The distance between the centre of gravity of the car body and the top of the rail	1520 mm
The distance between the frame of gravity of the car body and the top of the rail	510 mm
The longitudinal stiffness of the primary suspension steel spring	980 kN/m
The lateral stiffness of the primary suspension steel spring	980 kN/m
The vertical stiffness of the primary suspension steel spring	1176 kN/m
The vertical damping of the primary suspension	19.6 kN·s/m
The longitudinal stiffness of the second suspension air spring	158.76 kN/m
The lateral stiffness of the second suspension air spring	158.76 kN/m
The vertical stiffness of the second suspension air spring	189.14 kN/m
The lateral damping of the second suspension	58.8 kN·s/m
The lateral damping of the second suspension	40 kN·s/m
The longitudinal stiffness of the traction rod	7882.6 kN/m
The lateral stiffness of the traction rod	16 kN/m
The vertical stiffness of the traction rod	16 kN/m

Table 2 DOFs used in the vehicle multi-body system components for a single vehicle

	Longitudinal	Lateral	Vertical	Roll	Pitch	Yaw
Car body	X_c	Y_c	Z_c	ϕ_c	β_c	ψ_c
Bogie frame (i=1,2)	X_{bi}	Y_{bi}	Z_{bi}	ϕ_{bi}	β_{bi}	ψ_{bi}
Wheelset (i=1,2,3,4)	X_{wi}	Y_{wi}	Z_{wi}	ϕ_{wi}	β_{wi}	ψ_{wi}

2.2.2 Track model and wheel/rail contact

Because the aim of the present study is to investigate the dynamic performance of a multi-body vehicle with respect to unsteady aerodynamic forces, the vibrations of the structures at the bottom of the track, such as the supporting block, are neglected here. The track model used in this study is inertia fixed rails, with a nonlinear contact between the wheel and rail. Kalker's (1982) simplified nonlinear theory is used to calculate the contact force, and the creep forces are calculated using the position of the contact partners as well as their velocities and relative velocities. Considering an ideal dry wheel/rail contact, a friction coefficient of 0.4 is used in this study. In addition, the low-interference spectrum is adapted for the high-speed railway of 250 km/h or more (Zhai 2014), and considering the design speed of Lanzhou-Xinjiang high-speed railway is more than 250 km/h, meanwhile, it is a newly-built line recently, the wear and interference to track is less. Therefore, the high-speed low-interference track spectrum (supplied by SIMPACK) is used to consider the impact of track irregularity.

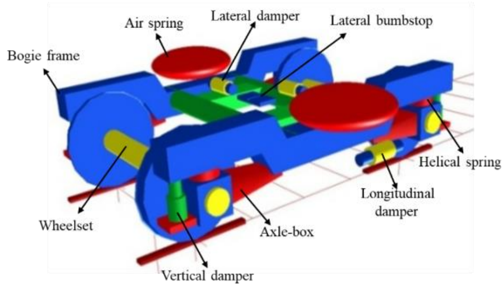

(a) Bogie model

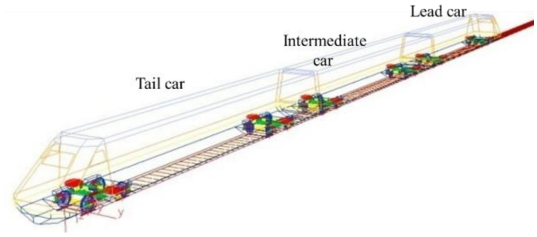

(b) Vehicle model

Fig. 6 The vehicle dynamic model

2.3 The wind-loaded vehicle system model

To investigate the dynamic response performance of the vehicle with respect to the unsteady aerodynamic forces, this section establishes a wind-loaded vehicle system model based on the vehicle aerodynamic model and vehicle system dynamic model, as shown in the calculation flow chart in Fig. 7. First, establish the vehicle and actual landform aerodynamic model, then obtain the unsteady aerodynamic forces and moment through the CFD analysis. Second, establish the vehicle system dynamic model in SIMPACK according to the actual parameters. Third, put the aerodynamic forces and moments time histories into the vehicle dynamic model by the data input module in SIMPACK, and then the wind-loaded vehicle system model generated. Concretely, the aerodynamic forces, including lateral force, lift force, roll moment, pitch moment and yaw moment, are applied to the vehicle. Corresponding to the locations of the aerodynamic results, the action point of the lateral force F_{wy} is the centre of the car body side wall; the action point of the lift force F_{wz} is the centre of the car body underside; and the action points of the roll moment m_{wx}, pitch moment m_{wy}, and yaw moment m_{wz} are all at the centre of gravity of the car body. Finally, the vehicle attitude and dynamic response change under unsteady aerodynamic forces can be obtained.

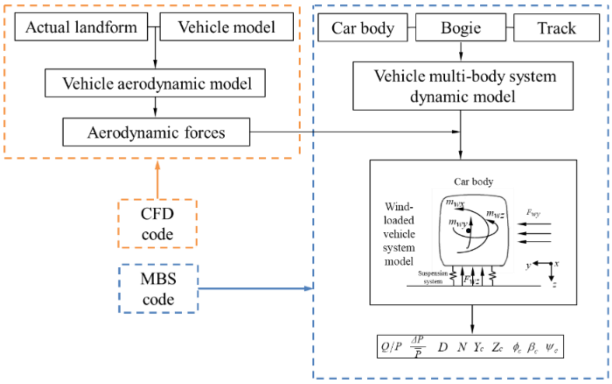

Fig. 7 The calculation flow chart of the wind-loaded vehicle model

In addition, corresponding to the CFD calculation process, the wind loads are simultaneously applied to the lead, middle and tail car. When importing the CFD wind load data into the dynamic vehicle system in SIMPACK, the vehicle system dynamic computational time should be consistent with the wind load variation time. However, the timely interaction between the vehicle motion and the wind is not considered in this work. When the vehicle runs in the shelter of the uniform windbreak wall, the effect of wind is effectively reduced, and the wind load acts on the vehicle is slight and steady, so the vehicle runs safely. While in the transition region of the windbreak, the wind load changes quickly, and the influence of the wind load on the vehicle is more significant than the vehicle motion response to the wind. For example, in the full-scale test, the maximum roll angle is not larger than 2.0° in the transition region, namely, the changes of the side area and volume of a single car is not larger than 0.056 m^2 and 0.00363 m^3, and the ratio between the force generated by the change of the air volume and the sudden wind load is less than 8×10^{-6}. It can be seen that the wind load variation induced by the vehicle motion posture is few compared to the sudden wind load itself. Therefore, neglecting the interaction between the vehicle motion and the wind in the time domain is acceptable in this study.

3. Method validation

3.1 Description of the full-scale test methodology

Based on machine vision, a vehicle vibration displacement and attitude measurement system that consists of four sets of high-speed charge-coupled devices (CCDs) and a line laser has been researched and developed by the authors' laboratory, as shown in Fig. 8(a). The four sets of high-speed CCDs are installed under the car body in positions that are not collinear. The structural flow chart of the measurement system is shown in Fig. 8(b). First, these four measurement devices are controlled by the synchronizing signal trigger to achieve synchronous data acquisition; then, image acquisition and processing is executed by the lower industrial personal computer (IPC).

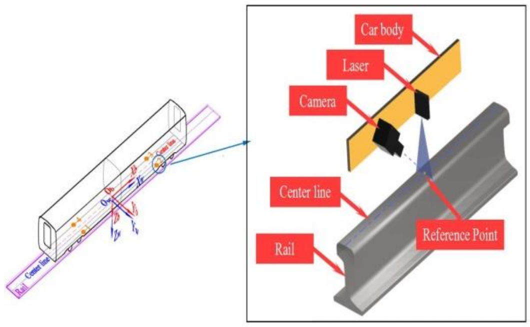

(a) A sketch of the measurement system

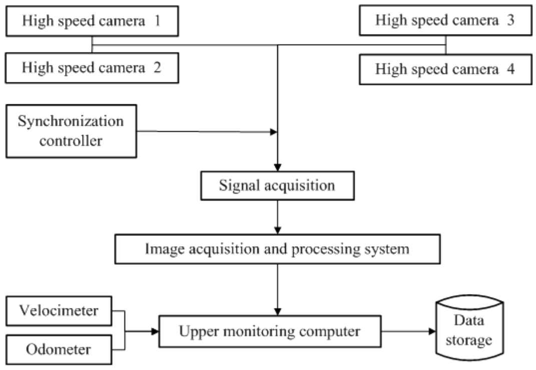

(b) The structural flow chart of the measurement system

Fig. 8 The car body motion attitude measurement system

The processing results are sent to the upper monitoring computer, and the vehicle motion attitudes are obtained by the detection program. The sampling rate is 260 Hz, the analysis of data and detailed description of test principle and process can refer to Liu *et al*. (2017) In addition, the vehicle-mounted global positioning system (GPS) and the ground environment anemometer are used to obtain other information, such as vehicle speed, mileage and wind speed.

3.2 Comparison of the simulation and experimental results

Using the test method described above, the full-scale test in field, six conditions of the lead car passing the windbreak transition region, as shown in Table 3, are chosen to validate the computation method. The maximum lateral displacement and roll angle of the lead car's centre of gravity are obtained using the measurement system introduced above. In addition, as shown in Fig. 9, the wind speed and direction are obtained using the ground environment anemometer. The wind speed information presented in Table 3 is the average value. Based on the full-scale test conditions and results, the simulation and full-scale test results are compared and analysed.

In Table 3, V_t is the vehicle speed, V_w is the wind velocity, θ_w is the wind angle. The wind direction is defined as 0° in the north direction, with clockwise rotation being positive and anticlockwise rotation as negative.

Fig. 10 shows the results of the simulation and the full-scale test, with respect to the maximum lateral displacement

Y_{cmax} and roll angle ϕ_{cmax} of the lead cars' centre of gravity. It seems that the trend of the numerical simulation results and the experiment results is close but there are some errors, and the maximum error between them is 13%. This may due to a difference between the simulation and the experiment in the aspect of model simplification, turbulence intensity, randomness of wind and track irregularity. Considering the complexity of the field and the effects mentioned above, the error between the results is acceptable here.

4. Results and discussions

4.1 Dynamic responses of the vehicle

4.1.1 Safety criteria

In this study, the derailment coefficient, rate of wheel load reduction, and overturning coefficient are analysed in response to the unsteady aerodynamic forces. In addition, to directly reflect the vehicle motion in a crosswind environment, the vehicle vibration displacement, vibration angle, and vibration acceleration are also analysed.

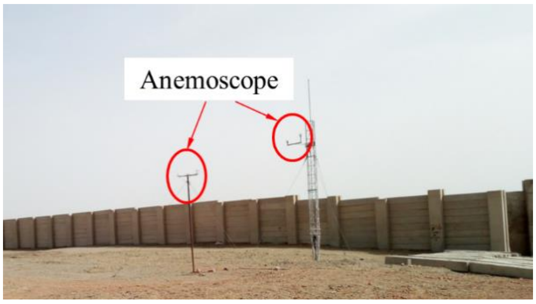

Fig. 9 Wind speed measurement

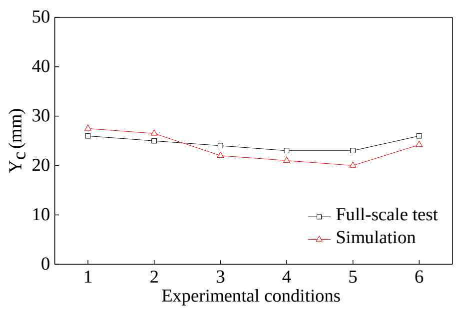

(a) Lateral displacement

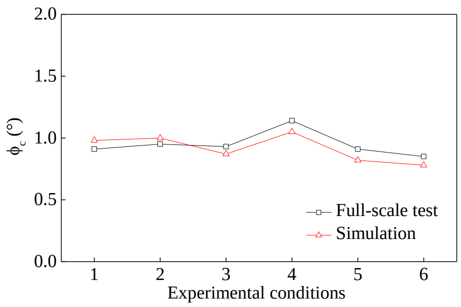

(b) The roll angle

Fig. 10 Results of the full-scale test and simulation

Table 3 Dynamic response parameters of the lead car in the full-scale test

Conditions	V_t (km/h)	V_w (m/s)	θ_w (°)	$Y_{c_{max}}$ (mm)	$\phi_{c_{max}}$ (°)
1	140	19	347	26	0.91
2	150	17.8	348	25	0.95
3	180	14.8	344	24	0.93
4	200	16.9	349	23	1.14
5	210	17.9	344	23	0.91
6	220	15.5	353	26	0.85

The derailment coefficient is the rate of lateral force Q and vertical force P at the contact point of the wheel and track, which reflects the probability that the wheel flange climbs above the rail top. According to the standards of the Design Specification of China High-Speed Railway (TB10621 2010), for design train speeds between 250 and 350 km/h, the derailment coefficient is defined as follows

$$Q/P \le 0.8 \tag{4}$$

The rate of wheel load reduction is the rate of the load reduction on one side of the wheel ΔP and the average static wheelset load $\overline{P}$. According to the Test Specification for Whole Train of China High-Speed EMU (Railway Transportation 2008), at a design speed greater than 200 km/h, the rate of wheel load reduction is defined as follows

$$\frac{\Delta P}{\overline{P}} \le 0.65\ (quasistatic)$$
$$\frac{\Delta P}{\overline{P}} \le 0.8\ (dynamic) \tag{5}$$

The overturning coefficient is used to assess whether the vehicle will overturn under crosswind force, centrifugal force and lateral vibration inertial force, the overturning coefficient is defined as follows (Hu 2009)

$$D < 0.8 \tag{6}$$

4.1.2 Dynamic response analysis under unsteady aerodynamic forces

Fig. 11 shows the wind load history on the train. To obtain a steady initial state for the dynamic wind-load vehicle computation in SIMPACK, no aerodynamic forces are applied on the vehicle before 3.25 s. Then, aerodynamic forces are loaded from 3.25 s to 9.75 s, and when the transient aerodynamic loads are applied on the car body completely, the wind loads are linearly unloaded from 9.75 s to 13 s. It can be seen that the aerodynamic forces are relatively stable in the cutting and embankment; however, when the vehicle passes through the rectangular transition region of a windbreak structure from the cutting to the embankment under a crosswind, the aerodynamic forces and moments fluctuate dramatically for a short time. Therefore, the dynamic responses of the vehicle are aggravated in this region.

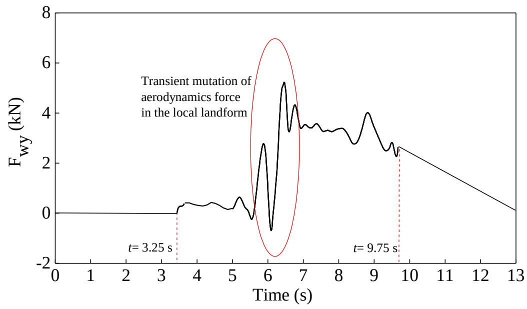

(a) Lateral force

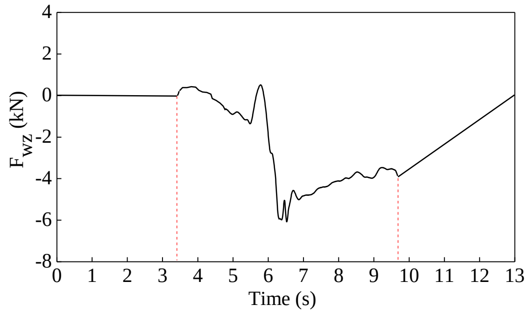

(b) Lift force

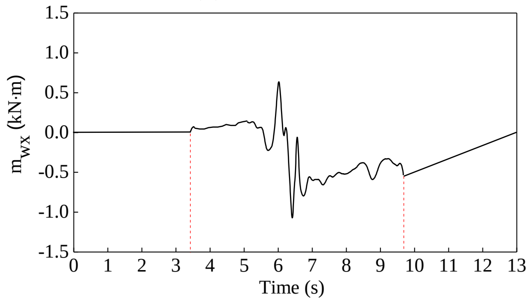

(c) Roll moment

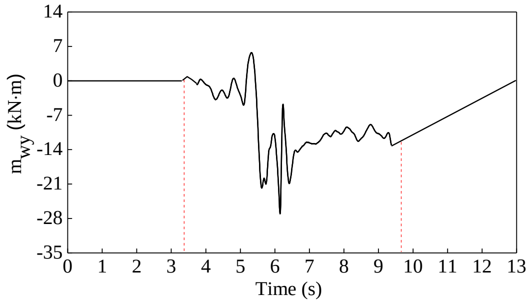

(d) Pitch moment

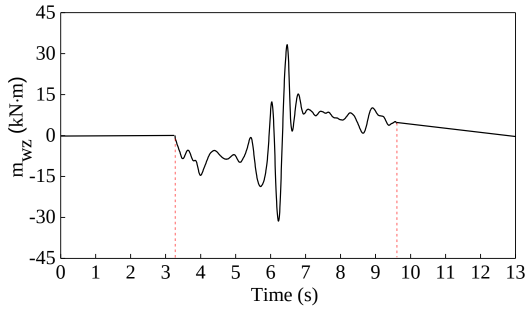

(e) Yaw moment

Fig. 11 Time history curves of the characteristic aerodynamic forces

Under a crosswind, the dynamic performance of the lead car is generally the worst. Therefore, the rest of the discussion in this section focuses on the lead car, unless otherwise specified. Based on the wind-loaded vehicle model, the dynamic responses for a vehicle speed of 250 km/h speed and a wind velocity of 30 m/s are analysed firstly. Fig. 12 shows the time history of the dynamic responses when the vehicle passes from the cutting to the embankment. The times plotted in the figure represent the main transient changes in the time period. The vehicle dynamic response has a similar profile as that of the wind load time history described in Fig. 11. Except for the effect of track irregularity, there are two main mutational peak values for every response parameter as the vehicle passes the rectangular transition region. The time history curves show that the unsteady aerodynamic forces greatly influence the dynamic responses of the vehicle. The dynamics parameters are relatively steady before the vehicle arrives at the rectangular transition region. Then, a strong transient response occurs when the train passes the rectangular transition. After the vehicle leaves the transition region, the dynamic responses gradually become steady again. However, every dynamic response index decays differently with time. The derailment coefficient decays the fastest, because it is obtained from one wheel, whereas the rate of wheel load reduction is obtained from a pair of wheelsets; the overturning coefficient is obtained from all of the wheelsets for the vehicle. In addition, for the wheel/rail normal force in Fig. 12(d), the left wheel and the right wheel have exactly opposite tendencies: the left wheel load decreases, whereas the right wheel load increases. The amplitude of the wheel load reduction is greater than that of the wheel load increase. Fig. 12(a) shows that the vehicle left side is close to the windbreak, indicating less crosswind resistance in the rectangular transition region than in the cutting and embankment. Therefore, the unsteady aerodynamic forces in this region can lead to a very strong negative effect on the dynamic performance of the vehicle.

Figs. 13(a) and 13(b) show the time history of the vibration displacement and the angle of the centre of gravity for the vehicle as it passes from the cutting to the embankment. In terms of the vibration displacement, the amplitude of the lateral vibration displacement Y_c is much larger than that of the vertical vibration displacement Z_c: the lateral vibration displacement peak value is 34 mm, whereas the vertical vibration displacement peak value is 9 mm. Furthermore, the lateral vibration takes longer to return to a steady state than the vertical vibration. In terms of the vibration angle, the roll angle ϕ_c, corresponding to the lateral vibration, is larger than both the pitch angle β_c and yaw angle ψ_c. The peak value of the roll angle is 1.2°, whereas the pitch and yaw angles are both less than 0.1°. However, in the transition region of the windbreak, the yaw angle has a stronger vibration than the roll angle and pitch angle under the unsteady aerodynamic forces. The amplitude changes in the lateral displacement, roll angle and yaw angle show that the unsteady aerodynamic forces caused by the local landform primarily influence the lateral motion of the car body.

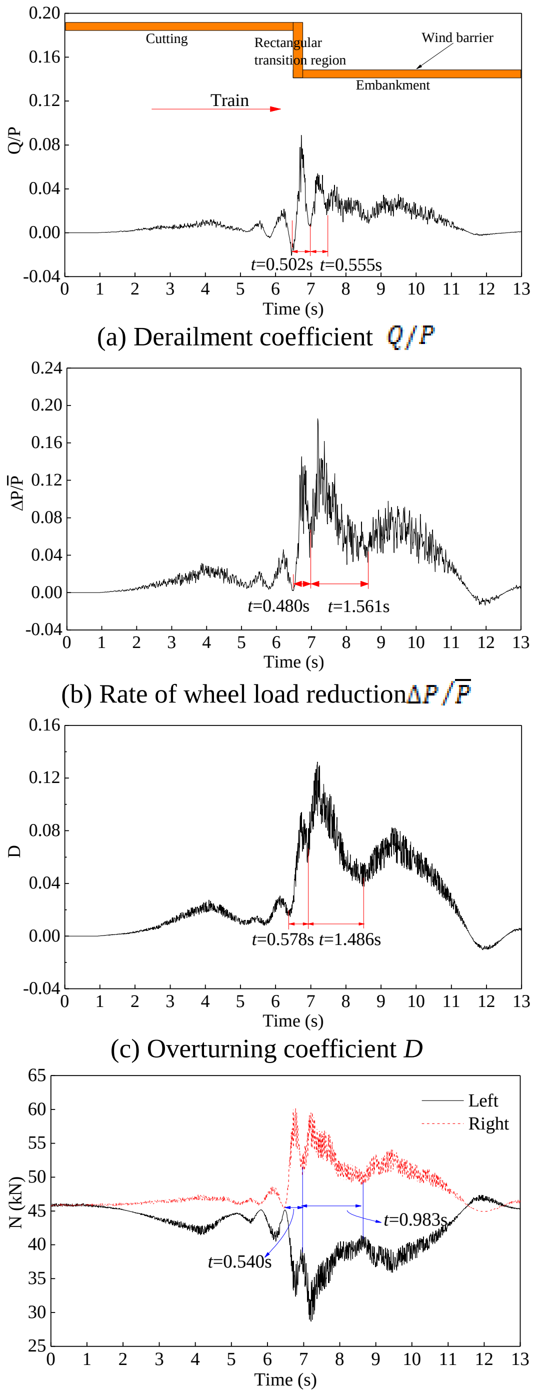

(a) Derailment coefficient Q/P

(b) Rate of wheel load reduction $\Delta P/\overline{P}$

(c) Overturning coefficient D

(d) Wheel/rail normal force N

Fig. 12 Time history curves of the vehicle dynamic response

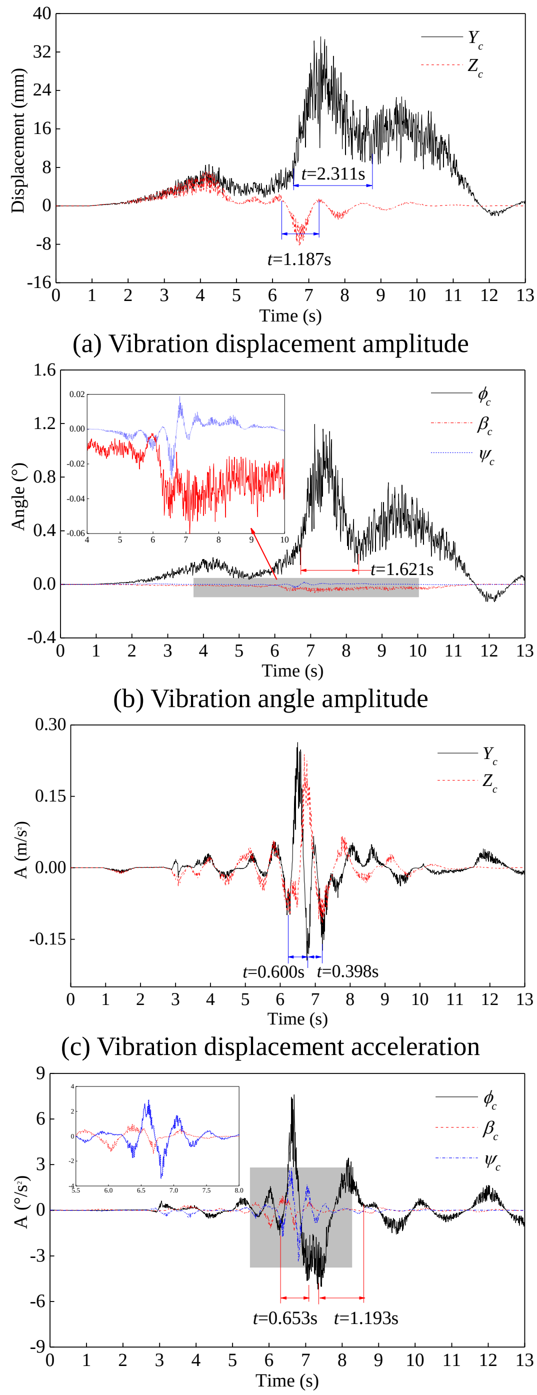

(a) Vibration displacement amplitude

(b) Vibration angle amplitude

(c) Vibration displacement acceleration

(d) Vibration angle acceleration

Fig. 13 Vehicle system vibration characteristics

The vibration displacement and angle show the vibration amplitude magnitude of the vehicle in response to the unsteady aerodynamic forces. Figs. 13(c) and 13(d) show the vehicle vibration acceleration, which is another important parameter that indicates the intensity of vibration and comfort level for the vehicle. It can be seen that the vibration frequency of lateral vibration acceleration is approximately twice as large as the vertical vibration acceleration. The intensity of the lateral vibration acceleration is slightly larger than that of the vertical vibration acceleration, which is different than the vibration displacement amplitude shown in Fig. 13(a). Therefore, although the amplitude of the vertical vibration is small, the intensity of the vertical vibration is not insignificant. For the angular vibration acceleration, the roll angle acceleration is the largest, the yaw angle acceleration is intermediate, and the pitch angle acceleration is the smallest. Overall, Fig. 13 indicates that the car body has a very strong roll motion and

Table 4 Amplitude and frequency of the dynamic response parameters

	Safety index			Vibration parameters				
	Q/P	$\Delta P/\bar{P}$	D	Y_c	Z_c	ϕ_c	β_c	ψ_c
Amplitude	0.112	**0.213**	0.147	**38.155**	10.835	**1.336**	0.057	0.033
Frequency	1.992	**2.083**	1.730	0.433	**0.842**	0.620	1.159	**2.049**

yaw motion as the vehicle passes the rectangular transition region. A 'sway' phenomenon appears briefly when the vehicle passes the rectangular transition region because of the unsteady aerodynamic forces caused by the landform.

To investigate the sensitivity of different dynamic parameters to the unsteady aerodynamic forces, the vibration amplitude (peak-peak value) and frequency of the eight dynamic response parameters discussed above are listed in Table 4. The frequency is obtained from the times in Figs. 12 and 13, and Table 4 shows the maximum frequency value. It can be seen that the rate of wheel load reduction, lateral vibration displacement and roll angle of the car body have the largest amplitudes. The rate of wheel load reduction, vertical displacement of the car body and yaw angle of the car body have the highest frequencies.

4.2 Effects of crosswind velocity and vehicle speed

4.2.1 Effect of crosswind velocity

The peak value variations of different dynamic parameters are analysed with a vehicle speed of 250 km/h as the crosswind velocity varies from V_w=10 m/s to 50 m/s. Fig. 14(a) shows the change in the vehicle safety index with increasing crosswind velocity. Overall, the rate of wheel load reduction is the largest, and the derailment coefficient is the smallest for every crosswind velocity condition. This phenomenon was also observed in other studies (Xia *et al*. 2009). The three safety indexes increase slowly when the crosswind velocity is less than 30 m/s; however, the peak values of the safety indexes increase rapidly when the crosswind velocity is greater than 35 m/s. When the crosswind velocity is greater than 40 m/s, the rate of wheel load reduction exceeds the safety level, and there is a risk of overturning when the crosswind reaches 45 m/s.

Figs. 14(b)-14(c) show that the crosswind velocity has a strong influence on the vehicle vibration performance. The lateral and vertical vibration displacements of the car body increase with increasing crosswind velocity. While the lateral vibration displacement is always larger than the vertical displacement, the lateral and vertical vibration displacements reach 74.5 mm and 18.1 mm, respectively, when the crosswind velocity is 45 m/s. Similar to the lateral displacement, roll motion also increases with increasing crosswind velocity. The roll angle increases rapidly and is 1.7° when the crosswind velocity is 45 m/s. However, the pitch angle and yaw angle increase slowly, with peak values of less than 0.1° from beginning to end.

4.2.2 Effect of vehicle speed

Considering a constant crosswind velocity of 30 m/s, which is the greatest wind speed that the vehicle allowed to enter the wind area in Lanzhou-Xinjiang railway; the vehicle speed is varied from V_t=120 km/h to 350 km/h. The effect of vehicle speed on the dynamic performance of the vehicle is investigated. Fig. 15(a) shows that the peak value of the vehicle operation safety indexes fluctuates with increasing vehicle speed. The rate of wheel load reduction is the largest, and the derailment coefficient is the smallest for every vehicle speed condition; however, every safety index is considered safe.

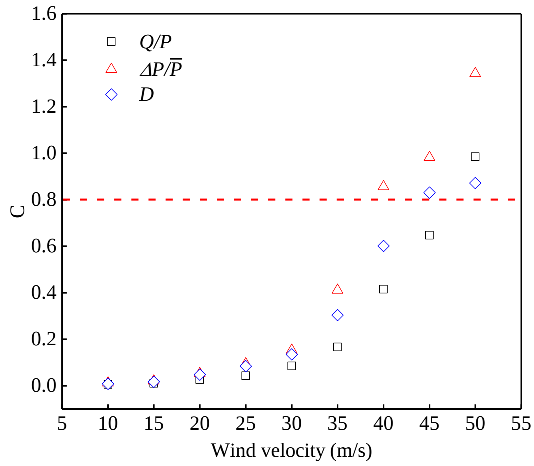

(a) The safety indexes

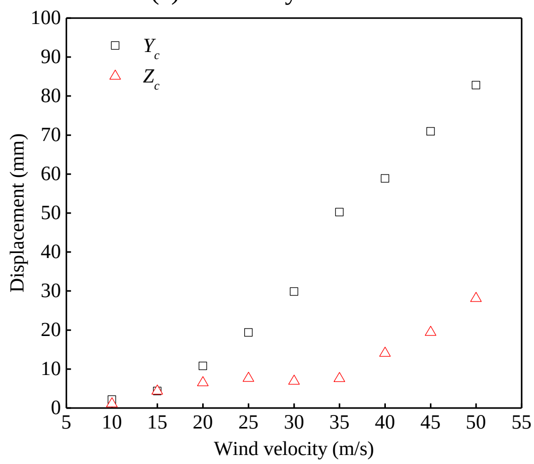

(b) Vibration displacement

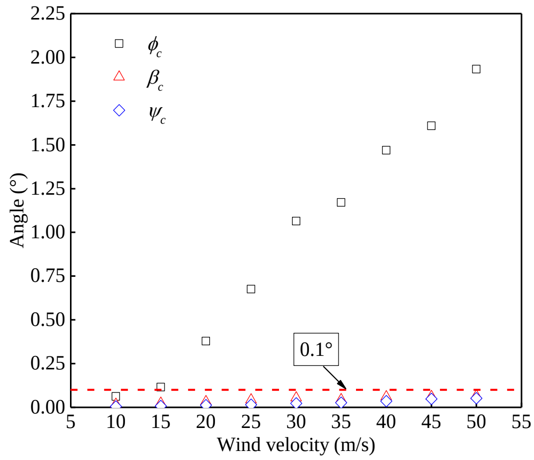

(c) Vibration angle

Fig. 14 Effect of crosswind velocity

The three safety indexes increase with increasing vehicle speed from 120 km/h to 250 km/h, when the vehicle speed is greater than 250 km/h, the three safety indexes decrease slightly. This occurrence maybe because of the co-vibration between the vibration induced by the unsteady aerodynamic forces and the inherent vibration of the vehicle. For example, as shown in Table 4, the roll frequency when the vehicle passes the rectangular transition region under the effect of unsteady aerodynamic forces is 0.62 Hz, which is close to the inherent frequency of the vehicle roll motion of 0.7 Hz (Lu *et al*. 2014). In this case, co-vibration appears easily.

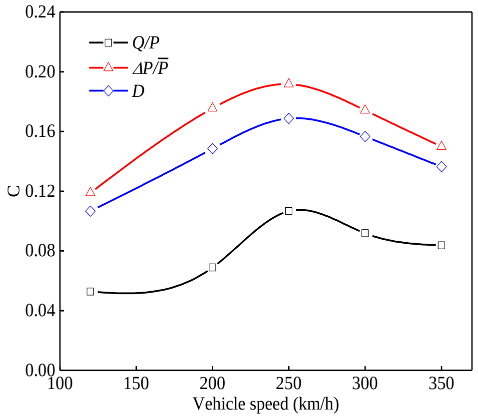

(a) The safety indexes

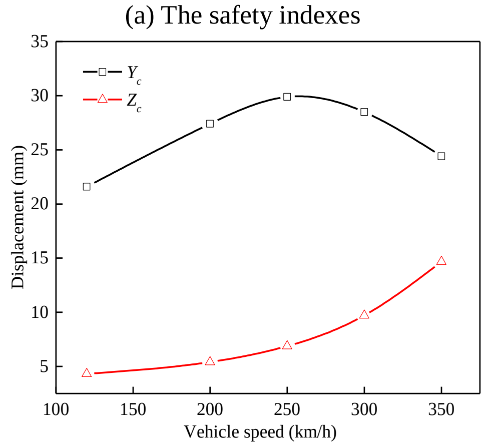

(b) Vibration displacement

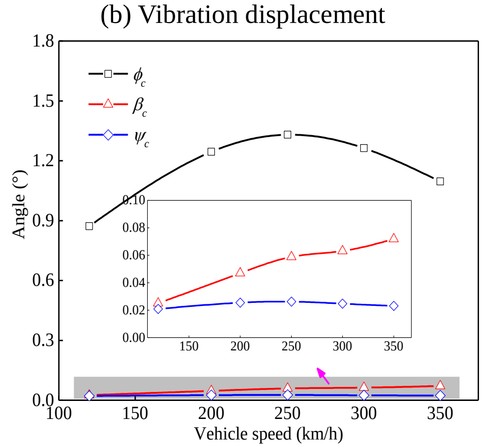

(c) Vibration angle

Fig. 15 Effect of vehicle speed

Figs. 15(b)-15(c) show the variations in the peak value of the vehicle vibration response parameters with vehicle speed. The lateral vibration displacement, roll angle and yaw angle are consistent with the three safety indexes discussed above. They all first increase and then decrease with increasing vehicle speed; this behaviour can also be attributed to the co-vibration phenomenon with respect to the lateral motion. The vertical vibration and pitch angle increase with increasing vehicle speed, but the peak values are not very large. The maximum values of the lateral and vertical vibration displacement are 29.9 mm and 14.7 mm, respectively; the maximum values of the roll angle, pitch angle and yaw angle are 1.33°, 0.71° and 0.03°, respectively. In summary, the crosswind velocity has a larger and more obvious influence on the dynamic performance of the vehicle than vehicle speed.

4.3 Discussion of the comparison with other works

The dynamic safety analysis of the train in the present work is similar to the computational model in the reference Liu *et al*. (2018). In the reference, the major work focused on the change of the aerodynamics of the train runs from the cutting to embankment, and explained the reason why the flow field and the aerodynamic forces of the train in the transition of the windbreak are worse. Finally, the authors used the three-mass model from the EN14067-6 (2010), and found that the safety assessment of the wheel unloading ratio $f_{\Delta Q}$ for a train is larger than the limitation value when the wind speed reaches 50 m/s when the train speed is 250 km/h. In the present work, the aerodynamic analysis is used just to obtain the time-history curves of the aerodynamic forces and moments. The major work of the present study is based on the multibody system dynamics (MBS) and consider the structure relationship of the real train and total DOFs, to analyze the safety and the vibration characteristics of the train that impacted by the unsteady aerodynamic forces and moments. The results find that an overturning risk occurs when the crosswind is 45 m/s under the train speed at 250 km/h.

It can be seen that the critical wind speed under the same train speed is different between the reference (Liu *et al*. (2018)) and the present work, but they are relative near to each other. It indicates that the method of the three-mass model and MBS are all adapt to the analysis of the train safety under the crosswind. However, in terms of the three-mass model, due to the number of dynamic suspension parameters is less than that of MBS, so the results maybe conservative generally; but here the results of MBS in the present work is more conservative. The reason can be explained by the following items: (1) the case that three-mass model is more conservative than MBS generally occurs under the steady wind, but the present work is an unsteady and transient aerodynamic loads; (2) the aerodynamic forces and moments used in the reference are the peak values (Liu *et al*. (2018)), but in the present work, the entire time-history of wind loads is used in the MBS, and the repeated impacts on the train may result in the worse results; (3) the impact of track irregularity in MBS also can increase the safety risk. Overall, the method of

MBS is relative more accurately due to more comprehensively consideration of different parameters, but focus on different aims, the three-mass model sometimes is more conveniently and also can get the acceptable results.

In addition, there is another research (Liu *et al*. (2019)) studied the effect of wind speed variation on the dynamics of a high-speed train by using the MBS method. Based on the real wind speed curve, considered the ramp time (to measure the rate of change in the wind), peak wind speed at different mean wind speeds (to measure the amplitude of the change in the wind speed), and peak wind-speed duration time, the ideal wind speed curve was built to analyze the effect of different factors on the safety of the train. The authors finally obtained the critical wind speed curve (CWC) for the CRH2 high-speed train with respect to wind speed variation under train speed at 120 km/h~250 km/h. Different with the reference (Liu *et al*. (2019)), the present work is based on the actual landforms and obtain the wind speed curve and the unsteady loads, then the time-history of the dynamic response of the train, including the vibration and safety characteristics are analyzed. Overall, the present work can be a supplementary and more deeply study to the relative research with respect to the effect of unsteady wind loads on the train safety, including the reference Liu *et al*. (2018), Liu *et al*. (2019) and other studies.

5. Conclusions

In this paper, a wind-loaded vehicle system model based on vehicle aerodynamics and the multi-body vehicle dynamics is established and used to investigate the dynamic performance under the unsteady aerodynamic forces caused by local landforms. The following conclusions are obtained:

- The unsteady aerodynamic forces caused by the local landforms strongly influence the dynamic performance of the vehicle. When the vehicle passes the discontinuous windbreak rectangular transition region, the dynamic parameters strongly vary with the aerodynamic forces. After the excitation, the dynamic parameters require a long time to return to a stable state.
- In terms of the vehicle operation safety indexes, the wheel load reduction has the largest amplitude and frequency. In terms of the vehicle vibration characteristics, the lateral displacement and roll angle have the largest amplitude, while the vertical vibration and yaw angle have the largest frequency. A ‘sway’ phenomenon briefly appears when the vehicle passes the special rectangular transition region.
- The vehicle dynamic performance worsens as the crosswind velocity increases. An overturning risk occurs when the crosswind is 45 m/s, when the lateral vibration displacement of the car body is 74.5 mm, the roll angle is 1.7°. With increasing vehicle speed, the dynamic parameters of the lateral motion first increase and then decrease slightly. The reason for this change can be attributed to the co-vibration between the vibration induced by the unsteady aerodynamic forces and the inherent vibration of the vehicle. In addition, in this case, the crosswind velocity has a greater effect on the dynamic performance than the vehicle speed.

Acknowledgments

This work was supported by the National Key R&D Program of China (Grant No. 2017YFB1201304-17), the National Railway Administration of the People’s Republic of China (Grant No. KF2017-006), the graduate student independent innovation project in Central South University (Grant No. 2017zzts197), and China scholarship council (CSC, Grant No. 201806370043).

References

Avila-Sanchez, S., Pindado, S., Lopezgarcia, O. and Sanzandres, A. (2014), “Wind tunnel analysis of the aerodynamic loads on rolling stock over railway embankments: The effect of shelter windbreaks”, *Scientific World J*., **2014**(6), 421829. http://dx.doi.org/10.1155/2014/421829

Baker, C., Cheli, F., Orellano, A., Paradot, N., Proppe, C. and Rocchi, D. (2009), “Cross-wind effects on road and rail vehicles”, *Vehicle Syst. Dyn*., **47**(8), 983-1022. https://doi.org/10.1080/00423110903078794

Catanzaro, C., Cheli, F., Rocchi, D., Schito, P. and Tomasini, G. (2010), “High-speed train crosswind analysis: CFD study and validation with wind-tunnel tests”, *Proceedings of the International Conference on Engineering Conferences International*, Springer, Cham, September.

Cui, T., Zhang, W.H. and Sun, B.C. (2014), “Investigation of train safety domain in cross wind in respect of attitude change”, *J. Wind Eng. Ind. Aerod*., **130**, 75-87. https://doi.org/10.1016/j.jweia.2014.04.006

EN 14067-6 (2010), Railway applications – aerodynamics – part 6: Requirements and test procedures for cross wind assessment; Brussels.

GB 50009-2001 (2003), Load code for the design of building structures, China Architecture and Building Press; Beijing, China.

Guo, W.W., Xia, H. and Raid, K. (2015), “Aerodynamic effect of wind barriers and running safety of trains on high-speed railway bridges under cross winds”, *Wind Struct*., **20**(2), 213-236. http://dx.doi.org/10.12989/was.2015.20.2.213

Hosoi, T. and Tanifuji, K. (2012), “Influence of cross wind on derailment of railway vehicle running on curved track at low speed”, *Int. J. Railway*., **77**(774), 381-391. https://doi.org/10.1299/jsmeacmd.2010.5._62961-1_

Hu, Y.S. (2009), *Modern Railway Vehicle Dynamics*, China Railway Publishing House, Beijing, China.

Huang, B.C and Wang, C.J. (2008), *Principle and application of structural wind resistance analysis*, Tongji University Press, Shanghai, China.

Iwnicki, S. (2006), *Handbook of railway vehicle dynamics*, CRC press.

Kalker, J.J. (1982), “A fast algorithm for the simplified theory of rolling contact”, *Vehicle Syst. Dyn*., **11**(1), 1-13. https://doi.org/10.1080/00423118208968684

Liu, D.R., Lu, Z.J., Cao, T.P. and Li, T. (2017), “A real-time posture monitoring method for rail vehicle bodies based on machine vision”, *Vehicle Syst. Dyn*., **55**(6), 853-874. https://doi.org/10.1080/00423114.2017.1284339

Liu, D.R., Wang, Q.X., Zhong, M., Lu, Z.J., Wang, J.B., Wang, T.J. and Lv, S.Y. (2019), “Effect of wind speed variation on the dynamics of a high-speed train", *Vehicle System Dynamics*, **57**(2), 247-268. https://doi.org/10.1080/00423114.2018.1459749

Liu, TH., Chen, Z.W., Zhou, X.S. and Zhang, J. (2018), "A CFD analysis of the aerodynamics of a high-speed train passing through a windbreak transition under crosswind", *Eng. Appl. Comput. Fluid Mech*., **12**(1), 137-151. https://doi.org/10.1080/19942060.2017.1360211

Liu, T.H., Su, X.C., Zhang, J., Chen, Z.W. and Zhou, X.S. (2016), "Aerodynamic performance analysis of trains on slope topography under crosswinds", *J. Central South University*., **23**(9), 2419-2428. https://doi.org/10.1007/s11771-016-3301-z

Lu, Z.J., Zhou, D., Zhou, W., Xiong, X.H. and Yang, M.Z. (2014), "Report of CRH2 full-scale test under the wind in Lanzhou-Xinjiang second double line", High-speed Train Research Centre, Central South University, Changsha, China.

Niu, J.Q., Zhou, D. and Li, Z.W. (2015), "Unsteady aerodynamic performance of high-speed train on local geomorphology under strong wind", *J. Central South University* (*Science and Technology*), **46**(6), 2359-2365.

Ogueta-Gutiérrez, M., Franchini, S. and Alonso, G. (2014), "Effects of bird protection barriers on the aerodynamic and aeroelastic behavior of high speed train bridges", *Engineering Structures*., **81**, 22-34. https://doi.org/10.1016/j.engstruct.2014.09.035

Pombo, J., Ambrã³Sio, J., Pereira, M., Rauter, F., Collina, A., and Facchinetti, A. (2009), "Influence of the aerodynamic forces on the pantograph–catenary system for high-speed trains", *Vehicle Syst. Dyn*., **47**(11), 1327-1347. https://doi.org/10.1080/00423110802613402

Pope. S.B. (2000), *Turbulent Flows*, Cornell University, New York, USA.

Railway Transportation-2008(8) (2008), Test Specification for Whole Train of China High-Speed EMU, Ministry of Railways of the People's Republic of China; Beijing, China.

TB10621-2009 (2010), Design Specification of China High-Speed Railway (for trial purpose), China Railway Publishing House; Beijing, China.

Thomas. D., Berg, M. and Stichel, S. (2010), "Measurements and simulations of rail vehicle dynamics with respect to overturning risk", *Vehicle System Dynamics*., **48**(1), 97-112. https://doi.org/10.1080/00423110903243216

Wang, B., Xu, Y.L. and Li, Y.L. (2015), "Dynamic analysis of wind-vehicle-bridge systems using mutually-affected aerodynamic parameters", *Wind Struct*., **20**(2), 191-211. https://doi.org/10.12989/was.2015.20.2.191

Wu, M.X., Li, Y.L. and Chen, N. (2015), "The impact of artificial discrete simulation of wind field on vehicle running performance", *Wind Struct*., **20**(2), 169-189. https://doi.org/10.12989/was.2015.20.2.169

Wu, M.X., Li, Y.L. and Zhang, W. (2017), ".Impacts of wind shielding effects of bridge tower on railway vehicle running performance", *Wind Struct*., **25**(1), 63-77. https://doi.org/10.12989/was.2017.25.1.063

Xiang, J., He, D. and Zeng, Q.Y. (2009), "Effect of cross-wind on spatial vibration responses of train and track system", *J. Central South University*, **16**(3), 520-524. https://doi.org/10.1007/s11771−009−0086−3

Xiao, X.B., Jin, X.S., Wen, Z.F., Zhu, M.H. and Zhang, W.H. (2011), "Effect of tangent track buckle on vehicle derailment", *Multibody Syst. Dyn*., **25**(1), 1-41. https://doi.org/10.1007/s11044-010-9210-2

Yakhot, V. and Orszag, S.A. (1986), "Renormalization group analysis of turbulence: I. Basic theory", *J. Sci. Comput*., **1**(1), 1-51. https://doi.org/10.1007/BF01061452

Zhai, W.M. (2014), *Vehicle-Track Coupled Dynamics* (4^{th} *Ed.*), *Volume 1*, Science Press, Beijing, China.

Zhai, W.M., Wang, K. and Cai, C. (2009), "Fundamentals of vehicle–track coupled dynamics", *Vehicle Syst. Dyn*., **47**(11), 1349-1376. https://doi.org/10.1080/00423110802621561

Zhai, W.M., Yang, J.Z. and Li, Z. (2015), "Dynamics of high-speed train in crosswinds based on an air-train-track interaction model", *Wind Struct*., **20**(2), 143-168. http://dx.doi.org/10.12989/was.2015.20.2.143

Zhang, T., Xia, H. and Guo, W.W. (2013), "Analysis on running safety of train on bridge with wind barriers subjected to cross wind", *Wind Struct*., **17**(2), 203-225. http://dx.doi.org/10.12989/was.2013.17.2.203

Zhang, N., Ge, G.H. and Xia, H. (2015), "Dynamic analysis of coupled wind-train-bridge system considering tower shielding and triangular wind barriers", *Wind Struct.*, **21**(3), 311-329. http://dx.doi.org/10.12989/was.2015.21.3.311

CC